Optimization for energy absorption of 3-dimensional tensegrity lattice with truncated octahedral units

Jingyao Zhang*[a], Makoto Ohsaki[a], Julian J. Rimoli[b], Kosuke Kogiso[a]

[a] Department of Architecture and Architectural Engineering, Kyoto University

Kyoto-Daigaku Katsura, Nishikyo, Kyoto 615-8540, Japan

[b] School of Aerospace Engineering, Georgia Institute of Technology, Atlanta, GA 30332, USA

* Corresponding author: zhang@archi.kyoto-u.ac.jp

Abstract

Tensegrity structures have recently found new applications as energy absorbers in the field of aerospace engineering. In this study, we introduce an optimization method to maximize the energy absorption capability of a 3D tensegrity lattice composed of truncated octahedral units. The stored strain energy of the tensegrity lattice subjected to forced vertical displacement is maximized under constraints on the stress, structural material volume, and volume occupied by the lattice. The force density of the bar that defines the shape of each unit is regarded as a parameter, and the design variables are the cross-sectional areas of cables and bars as well as the level of prestresses on the lattice. Buckling of the bars is extensively utilized to significantly increase energy absorption. The nonlinear behavior of bars allowing buckling is modeled as a smoothed function of bi-linear elastic material, in which imperfection in the bar shape is also taken into account. Numerical examples show that tensegrity lattices, with flexibility in the vertical direction and adequate (shear) stiffness in the horizontal direction, can be obtained by solving the optimization problem. It is also shown that energy absorption by the structure scales cubically when its sizes and prestress level are uniformly scaled.

Keywords: tensegrity lattice, optimization, strain energy, truncated octahedral unit, buckling

1. Introduction

Tensegrity structures are a class of self-standing pin jointed structures consisting of bars (struts) in compression and thin cables in tension [1]. Earlier research efforts focused on their form-finding [2] and stability [3], which are the two fundamental problems for the design of tensegrity structures. According to the strictest definition of tensegrity structures, which is also called class-1 tensegrity [4], the bars are usually not continuously connected, i.e., they are topologically isolated from each other. Isolation of the compressive members renders tensegrity structures particularly well suited for impact absorption applications, because the load-bearing capability of tensegrity structures remains intact even after undergoing severe deformation [5]. By exploiting their flexibility, tensegrity structures are utilized as devices for reducing impact forces [6], isolating dynamic forces [7], absorbing energy [8], and some other applications [9]. Among these, lattice structures consisting of tensegrity units have been also extensively studied to construct flexible large-scale systems [10, 11], of which wave-propagation properties were also studied [12].

In the field of aerospace engineering, tensegrity structures have been proposed as planetary landing devices, relying on their distinct properties: first of all, they are free-standing such that supports are unnecessary to maintain their stability; secondly, they are lightweight and can be packed into a small size to be launched from the earth; and finally, they can absorb energy from large impact loads to protect interior systems and payloads.

SunSpiral *et al.* [6] presented the concept of using a ball-like tensegrity probe to absorb significant impact forces, and to explore the planet as a surface mobility after landing by actively controlling its shape [13]. They further showed that the tensegrity probe may be able to operate on Titan with a science payload mass fraction of 50%, which is more than twice of the mass fraction of conventional devices, due to its multi-purpose usage.

Goyal *et al.* [8] demonstrated efficient energy absorption performance of the D-bar tensegrity system by comparison to that of a buckled bent beam with uniform full circular cross-section. The energy from external loads is stored as elastic energy in the members, for the purpose of avoiding local structural instabilities. This system exhibits an ability to store more energy than

the equivalent buckling-dominated system, but at the cost of significantly higher structural complexity.

Rimoli and Pal [9] presented a novel 3-dimensional tensegrity lattice, which is built from a combination of truncated octahedral unit cells via mirroring operations. They investigated the mechanical response of tensegrity lattices in the nonlinear regime, demonstrating that the structures have superior strength in the low-density regime attributed to the nonlinear geometric effects and buckling associated with the unit cell. It was then concluded that the tensegrity-based metamaterials are good candidates for energy absorption applications. Rimoli [5] further developed a reduced-order model to capture buckling and post-buckling behaviors of the bars as well as dynamic responses of tensegrity-based structures, when they are used as impact-tolerant components in planetary landers. By applying this model to the 3D tensegrity lattice, it was also shown that the structure exhibits multiple regimes with distinct behaviors, in a similar fashion to phase transitions in continuum systems [14, 15].

In the area of energy absorption, studies up to date mostly focus on presenting novel structural configurations and deformation regimes. There are only a few existing reports on optimizing their performance in energy absorption, although optimization methods have been mostly restricted to form-finding [16，17]. This motivates our current study on maximizing the energy absorption capability of a 3D tensegrity lattice assembled from truncated octahedral unit cells [9]. We study this 3D tensegrity lattice because of its 3D tiling property; i.e., it was the first lattice that can be easily extended to include much more unit cells in each of the three directions to construct a large-scale periodic structure. For the purposed of this study, we limit ourselves to the study of its elementary cell, consisting of eight truncated octahedral unit cells, which have threefold symmetry and are super-stable [18, 19] under certain conditions.

The objective function to be maximized is the strain energy under forced vertical displacement. Unlike some of the existing studies considering only global buckling [20] or reduced order model for local buckling, post-buckling behavior of the bars is analyzed in this study by recourse to a nonlinear elastic model, in which geometry imperfections of the bars are also taken into consideration.

The remainder of the paper is organized as follows. In Section 2 we introduce the basic properties and the configurations of the tensegrity lattice and its unit cells to be studied. The smooth formulation for post-buckling of bars and yield condition for a rectangular cross section are presented in Section 3. In Section 4 we formulate the optimization problem, followed by numerical case studies in Section 5. The conclusions of this work are laid out in Section 6.

2. Basic properties of truncated octahedral tensegrity lattice

The eight-unit tensegrity lattice studied in this paper is shown in Figure 1, where the thick and thin lines represent the bars in compression and cables in tension, respectively. The lattice is assembled from the regular truncated octahedral unit cells as depicted in [9], see Figure 2. Most of the bars of the lattice are topologically isolated, except for those connected to the nodes on the assembly boundary of different unit cells. For the completeness of the paper, this section presents some of the basic properties and the analytical conditions on self-equilibrium as well as stability of the truncated octahedral unit cells partially following our previous work [18].

Octahedron can be used for generating various types of tensegrity structures [21]. The vertices of a regular octahedron in Figure 2(a) are truncated by planes to generate the regular truncated octahedron in Figure 2(b). The cables of the truncated octahedral tensegrity are classified into the edge cables lying on the original edges of the truncated octahedron and the cutting cables lying on its cut edges. The bars are located inside of the truncated octahedron. Hence, a regular truncated octahedral tensegrity structure consists of 24 nodes, 12 bars, 24 cutting cables, and 12 edge cables, i.e., 48 members in total.

The prestresses at the self-equilibrated state are obtained in terms of force density, which is defined as the ratio of the member force to the member length. Denote the force densities of the edge cables, cutting cables, and bars as q_e, q_c, and q_b, respectively. Due to symmetry of the structure, members in each of three types have the same length and the same prestress, and accordingly, they have the same force density.
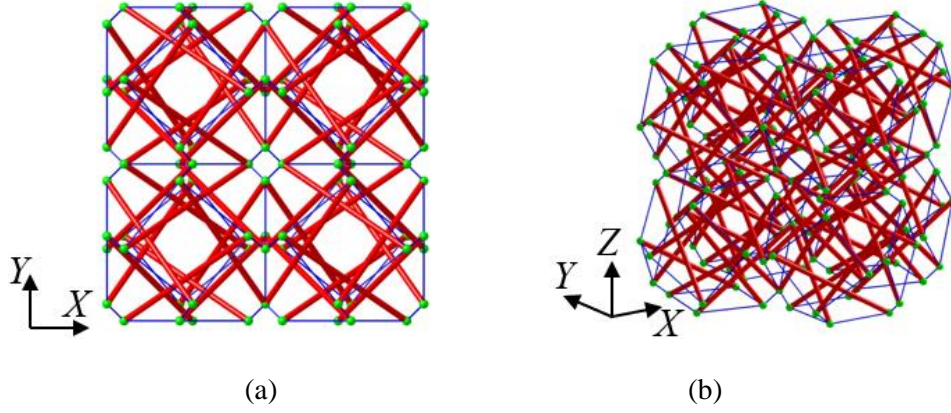
Figure 1. Undeformed shape of eight-unit tensegrity lattice;
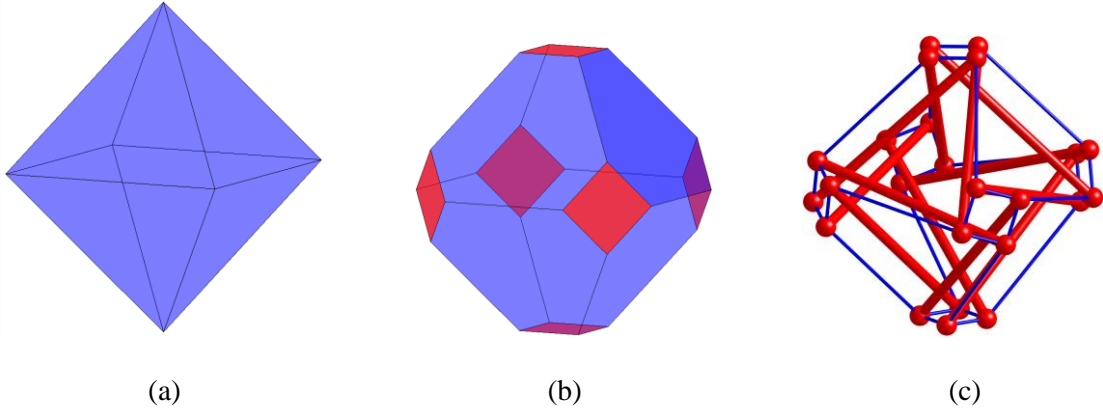(a) plan/elevation view, (b) diagonal view.

Figure 2. Generation of regular truncated octahedral tensegrity structure;
(a) regular octahedron, (b) truncated octahedron, (c) truncated octahedral tensegrity.

Let $\mathbf{E} \in \mathbb{R}^{24 \times 24}$ denote the force density matrix, for which the elements are linear functions of the force densities. The self-equilibrium equations in x-, y-, and z-directions are given as follows by using the coordinate vectors $\mathbf{x}$, $\mathbf{y}$, and $\mathbf{z}$ $\in \mathbb{R}^{24}$ [1, 2]:

$$\mathbf{Ex} = \mathbf{0}, \quad \mathbf{Ey} = \mathbf{0}, \quad \mathbf{Ez} = \mathbf{0} \tag{1}$$

Define η and ξ as

$$\eta = \frac{q_e + q_b}{2}, \quad \xi = \frac{q_e - q_b}{2} \tag{2}$$

Since the cables and bars are in tensile and compressive states, respectively, the force densities are positive in cables and negative in bars; therefore, $\xi > 0$ holds. For self-equilibrium of the

regular truncated octahedral tensegrity structure, we have the force density q_c of cutting cables solved as follows [18]:

$$q_c = \frac{\xi^2 - 5\eta^2 + \sqrt{\eta^4 + 14\eta^2\xi^2 + \xi^4}}{4\eta} \tag{3}$$

It is notable that when the level of prestresses in terms of force densities (q_e, q_c, q_b) is adjusted to $(\beta q_e, \beta q_c, \beta q_b)$ using a scaling parameter β, the self-equilibrium equations in Eq. (1) are satisfied by the same configuration in terms of nodal coordinates **x**, **y**, **z**, because the force density matrix **E** is simply scaled to β**E**. Furthermore, the self-equilibrium equations will not be violated with affine transformation of the initial symmetric self-equilibrated shape [3], which gives us the chance to study the structure without special caution on its scale.

The regular truncated octahedral tensegrity has only one prestress mode but 19 infinitesimal mechanisms. Furthermore, if $-1 < q_b / q_e < 0$ holds and member failure (cable yielding and bar buckling) is not considered, this structure is *super-stable*; i.e., it is always stable irrespective of the material properties as well as the level of prestresses [3].

Eight units of regular truncated octahedral tensegrity structures are combined to obtain the tensegrity lattice as shown in Figure 1. The units are transformed symmetrically with respect to the horizontal plane and the two vertical planes and connected on the planes of symmetry. Four nodes of each truncating section are connected to those of another symmetrically located unit, where one of the duplicated cutting cables on each plane are removed. Hence, the total number of members is $48 \times 8 - 4 \times 12 = 336$, including 96 struts, 96 edge cables, and 144 cutting cables. Note that 48 pairs of the cutting cables are shared by the two adjacent units, and the initial forces of these cutting cables are doubled to satisfy self-equilibrium equations after combing the duplicated cutting cables. The number of nodes of the eight-unit tensegrity lattice is 144 after removing the duplicated nodes on the planes of symmetry. Moreover, two bars of adjacent units may share a node on the internal boundary. Therefore, the tensegrity lattice is classified as class-2, although each unit is a class-1 tensegrity [4].

3. Large-deformation analysis of a bar under forced axial deformation

In this section, Euler buckling of a bar is incorporated for accurate simulation of large deformation of the tensegrity lattice. Formulations for post-buckling analysis and evaluation of maximum edge stress are presented for a single bar subjected to axial deformation.

3.1 Non-dimensional formulations for bilinear elastic bar buckling

Let P denote the axial force applied to one end of a simply supported bar of length L, cross-sectional area A, and cross-sectional moment of inertia I. The material of bar is assumed to have a linear elastic behavior with Young's modulus E. Let Δ be axial deformation of the bar. In the linear regime, P and Δ are related through the equation $P = k\Delta$, where $k = EA/L$ is the axial stiffness of the bar. The bar under compression buckles when P reaches the critical load determined by the Euler buckling load $P_{cr} = -\pi^2 EI / L^2$, when no geometry imperfection is considered. The negative sign for P_{cr} indicates that the critical (buckling) load is compressive.
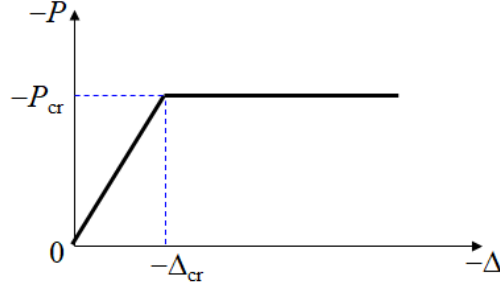
Figure 3. Bilinear elastic buckling model for axial force P and axial deformation Δ.

The simplest model for Euler buckling is a bilinear model as shown in Figure 3, where the axial force is constant after buckling (this is an approximation to the elastica solution, in which the post-buckling regime is dictated by elliptical integrals). This load-deformation relation for a bar can be expressed as

$$P(\Delta) = \begin{cases} P_{cr} & \text{if } \Delta < \Delta_{cr} \quad \text{(after buckling)} \\ k\Delta & \text{if } \Delta \geq \Delta_{cr} \quad \text{(before buckling)} \end{cases} \tag{4}$$

where Δ_{cr} (<0) is the critical axial deformation corresponding to the Euler buckling load $P = P_{cr}$ (<0). Here, we have

$$\Delta_{cr} = -\frac{\pi^2 I}{AL} \tag{5}$$

Assuming the bar remains in elastic range, this nonlinear behavior is purely attributed to geometrical nonlinearity, thus it is fully reversible. Consequently, for the forced axial deformation, the load-deformation relation can be expressed in terms of the potential energy $W(\Delta)$, which is the elastic strain energy in this case, such that $P(\Delta) = \mathrm{d}W(\Delta) / \mathrm{d}\Delta$.

For the sake of generality, we define the non-dimensional bar deformation $\eta \ (<0)$ as follows:

$$\eta = \frac{\Delta}{|\Delta_{cr}|} \tag{6}$$

from which we have the following equation for the case before buckling:

$$k\Delta = k \, | \Delta_{cr} | \frac{\Delta}{|\Delta_{cr}|} = | P_{cr} | \eta \tag{7}$$

Therefore, the load-deformation relation in Eq. (4) can be expressed as

$$P(\eta) = | P_{cr} | \, p(\eta), \text{ where } p(\eta) = \begin{cases} -1 & \text{if } \eta < -1 \\ \eta & \text{if } \eta \ge -1 \end{cases} \tag{8}$$

The nonlinear strain energy W is

$$W(\Delta) = \int P(\Delta)\mathrm{d}\Delta \tag{9}$$

Alternatively, the strain energy can be written in terms of the non-dimensional bar deformation η by changing variable as $\Delta = | \Delta_{cr} | \eta$:

$$W(\eta) = \int | P_{cr} | \, p(\eta) | \Delta_{cr} | \mathrm{d}\eta = | P_{cr} \Delta_{cr} | \int p(\eta)\mathrm{d}\eta = | P_{cr} \Delta_{cr} | \, w(\eta) \tag{10}$$

where $w(\eta)$ is the non-dimensional strain energy, which can be obtained as follows from integration for each region of η by assuming zero strain energy at the origin and continuity between different regions:

$$w(\eta) = \begin{cases} -\eta - \dfrac{1}{2} & \text{if } \eta < -1 \\[2mm] \dfrac{1}{2}\eta^2 & \text{if } \eta \geq -1 \end{cases} \tag{11}$$

Note that the corresponding bar force P and tangent stiffness K can be obtained by simple differentiation of $W(\eta)$ with respect to Δ using the chain rule.

3.2 Smooth model for post-buckling approximation

The piecewise definitions of the strain energy and the corresponding force-deformation relation, given in Section 3.1, can lead to both numerical and analytical challenges, when we analyze structures in nonlinear regimes with buckled bars. Moreover, imperfection in geometry of the bars has not been considered in the bilinear buckling model. Thus, we introduce a smooth elastic strain energy $\tilde{w}(\eta)$ that can serve as an approximation of Eq. (11) for the behavior of slender bars under compression:

$$\tilde{w}(\eta) = -\eta + \frac{1}{\gamma^2}\,\mathrm{dilog}(e^{\gamma}) - \frac{1}{\gamma^2}\,\mathrm{dilog}(e^{\gamma(\eta+1)} - e^{\eta\gamma} + 1) \tag{12}$$

where $\gamma > 0$ is a parameter for controlling the smoothness of the approximation around the critical point, and $\mathrm{dilog}(\cdot)$ is the dilogarithm function defined as

$$\mathrm{dilog}(\eta) = \int_1^{\eta} \frac{\ln(t)}{1-t}\,dt \tag{13}$$

We will now show that the approximation $\tilde{w}(\eta) \to w(\eta)$ when $\gamma \to \infty$. The first term on the right-hand side of Eq. (12) is independent of γ, and the second term is trivial when we take the limit $\gamma \to \infty$:

$$\lim_{\gamma \to \infty}\left(\frac{1}{\gamma^2}\,\mathrm{dilog}(e^{\gamma})\right) = -\frac{1}{2} \tag{14}$$

Thus, we have

$$\lim_{\gamma \to \infty}\tilde{w}(\eta) = -\eta - \frac{1}{2} - \lim_{\gamma \to \infty}\left(\frac{1}{\gamma^2}\,\mathrm{dilog}(e^{\gamma(\eta+1)} - e^{\eta\gamma} + 1)\right) \tag{15}$$

The value of the limit in the last term in Eq. (15) depends on the value of η, yielding

$$\lim_{\gamma \to \infty} \left(\frac{1}{\gamma^2} \operatorname{dilog}(e^{\gamma(\eta+1)} - e^{\eta\gamma} + 1) \right) = \begin{cases} 0 & \text{if } \eta < -1 \\ \dfrac{1}{2}\eta^2 + \eta + \dfrac{1}{2} & \text{if } \eta \geq -1 \end{cases} \tag{16}$$

Hence, we have the non-dimensional strain energy as

$$w(\eta) = \lim_{\gamma \to \infty} \tilde{w}(\eta) = \begin{cases} -\eta - \dfrac{1}{2} & \text{if } \eta < -1 \\ \dfrac{1}{2}\eta^2 & \text{if } \eta \geq -1 \end{cases} \tag{17}$$

and the approximated strain energy $\tilde{W}(\eta)$ is given as

$$\tilde{W}(\eta) = |P_{\text{cr}}\Delta_{\text{cr}}| \, \tilde{w}(\eta) \tag{18}$$

The corresponding approximated bar force $\tilde{P}(\eta)$ is obtained as follows:

$$\tilde{P}(\eta) = \frac{d\tilde{W}}{d\Delta} = \frac{d\tilde{W}}{d\eta}\frac{d\eta}{d\Delta} = \frac{d\tilde{W}}{d\eta}\frac{1}{|\Delta_{\text{cr}}|} = |P_{\text{cr}}| \, \tilde{p}(\eta) \tag{19}$$

where the non-dimensional approximate bar force $\tilde{p}(\eta)$ is given by

$$\tilde{p}(\eta) = \frac{d\tilde{w}(\eta)}{d\eta} = -1 + \frac{1}{\gamma}\ln(e^{\gamma(\eta+1)} - e^{\eta\gamma} + 1) \tag{20}$$

Analogously, the approximated tangent stiffness $\tilde{K}(\eta)$ is given by

$$\tilde{K}(\eta) = \frac{|P_{\text{cr}}|}{|\Delta_{\text{cr}}|}\tilde{k}(\eta), \text{ where } \tilde{k}(\eta) = \frac{d\tilde{p}}{d\eta} = \frac{e^{\gamma(\eta+1)} - e^{\eta\gamma}}{e^{\gamma(\eta+1)} - e^{\eta\gamma} + 1} \tag{21}$$

Note that the scalar $1/\gamma$ can be interpreted as a measure of imperfection of the beam. We can have smooth relations close enough to a perfect bar with bilinear relation when $1/\gamma$ is small enough. That is, the strain energy behaves as a perfect bar when the imperfection vanishes; i.e., $1/\gamma \to 0$. As $1/\gamma$ increases, the transition between the two regimes becomes smoother, as it is a beam with an imperfection.
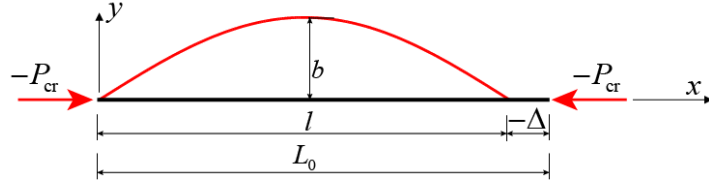
Figure 4. A buckled bar with sinusoidal curve.

3.3 Yield condition for a buckled bar

The approximation of the strain energy and consequent load and stiffness approximations included in the previous section do not require knowledge about the actual off-axis deformation of the beam after bulking. However, an estimation of such shape is required to determine the maximum stress experienced along the bent beam to establish realistic load (or deformation) limits in the optimization problem. In order to determine the relation between axial deformation and maximum stress on the beam we assume that the buckled bar has a sinusoidal shape as shown in Figure 4. In the large-deformation analysis of a slender bar, the critical deformation $|\Delta_{cr}|$ is small, and the change in the distance between the two end nodes is not significant. Therefore, we define the lateral deformation y of the buckled bar, based on the standard Lagrangian formulation, as a function of the axial coordinate x at the undeformed state as

$$y = b\sin\frac{\pi}{L_0}x, \quad (0 \le x \le L_0) \tag{22}$$

where b is the deformation in the middle of the buckled beam in y-direction. By numerically fitting lengths of the straight and curved bars, respectively, before and after buckling, we can find the relation between b and Δ.

It is obvious from Figure 4 that the maximum bending moment M occurs in the middle of the buckled bar, which is derived as

$$M = |P_{cr}|b \tag{23}$$

Moreover, the maximum absolute value of the stress σ_{max} exists at the compressive edge in the middle of the buckled bar; i.e., σ_{max} is computed using the section modulus Z_b as

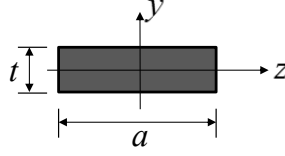$$\sigma_{max} = \frac{|P_{cr}|}{A} + \frac{M}{Z_b} \tag{24}$$

Figure 5. Rectangular cross section of a bar.

In this study, we consider the rectangular cross section as shown in Figure 5, which has the thickness t ($< a$) in y-direction and the width a in the perpendicular axis. The maximum stress σ_{max} is written as follows, since the beam deforms around the weak (y-)axis:

$$\sigma_{max} = \frac{\pi^2 Ebt^3 / (12L_0^2)}{bt} + \frac{[\pi^2 Ebt^3 / (12L_0^2)]b}{bt^2 / 6} = \frac{\pi^2 Et(t + 6b)}{12L_0^2} \tag{25}$$

To guarantee the buckled bar remains in the elastic range, we have the following constraint on σ_{max}

$$\sigma_{max} \leq \sigma_y \tag{26}$$

where σ_y is the yield stress of the material. In the following optimization problem, we vary the width a in proportion to the cross-sectional area A with a fixed thickness t. Hence, we have the following inequality constraint for the lateral deformation b of each bar:

$$b \leq \hat{b} = \frac{2\sigma_y L_0^2}{\pi^2 Et} - \frac{t}{6} \tag{27}$$

4. Formulation of optimization problem

In the optimization problem, the objective function is the strain energy S stored in the tensegrity lattice, before any bar yields violating Eq. (26) or Eq. (27). Here, for simplicity, the strain and stress due to initial prestress is included in evaluation of the total strain energy. A small value is assigned for the radius of gyration of the bar section so that Euler buckling precedes the yielding of a bar.

As explained in Section 2, the shape of a tensegrity is determined by the force densities only. The force density q_b (< 0) of the bars, with a fixed value $q_e = 1.0$ for the edge cables, is varied as a parameter to change the shape of the tensegrity lattice, but it is not considered as a design variable in this study; and therefore, the undeformed shape does not change during the optimization process. Let the nominal volume of the structure denote the volume of the smallest cuboid in which the structure is inscribed. The scales of the tensegrity lattices corresponding to various values of q_b are specified so that they have the same nominal volume.

The cross-sectional areas of bars and cables are denoted by A_b and A_c, respectively, and they are chosen as design variables. Let L_b and L_c denote the total lengths of bars and cables, respectively. The constraints are given as follows so that the total material volume does not change from its initial volume V_0:

$$A_b L_b + A_c L_c = V_0 \tag{28}$$

Another design variable is the scaling coefficient β representing the level of prestresses. It is multiplied to the axial forces of all members at the initial undeformed state derived from the self-equilibrium analysis in Section 2.

The optimization problem for finding A_b, A_c, and β to maximize the total strain energy $S(A_b, A_c, \beta)$ stored before any bar yields is formulated as

$$
\begin{aligned}
& \text{Maximize } S(A_b, A_c, \beta) \\
& \text{subject to } A_b L_b + A_c L_c = V_0 \\
& \qquad\qquad A_b^L \le A_b \le A_b^U \\
& \qquad\qquad A_c^L \le A_c \le A_c^U \\
& \qquad\qquad \beta^L \le \beta \le \beta^U
\end{aligned}
\tag{29}
$$

where the superscripts 'U' and 'L' indicate the upper and lower bounds of the variables.

Note that size of the lattice can be scaled uniformly after obtaining an optimal solution for the predefined size. Suppose the dimension of the lattice is scaled by the factor s; i.e., the length L_0, the thickness t, and the width a are respectively scaled to sL_0, st, and sa. Accordingly, the cross-sectional areas A_b and A_c become $s^2 A_b$ and $s^2 A_c$, respectively. Moreover, the tangent stiffness matrix $\mathbf{K}$ becomes $s\mathbf{K}$, if the specified stress level is also scaled by s to $s^2 \beta$. From

Eq. (27), the upper bound deflection $\hat{b}$ of the bar becomes $s\hat{b}$, leading to the fact that the maximum stress σ_{max} in Eq. (25) does not change. Hence, β becomes $s^2\beta$, and the reaction force is multiplied by s^2. The stored strain energy S becomes s^3S, since the scale for the displacement and axial deformation is s. On the other hand, when the specified material volume V_0 is scaled by the factor s for the lattice with the fixed force density q_{b}, the optimal values of the prestress level β and cross-sectional areas A_{b} and A_{c}, and consequently, the reaction force and the stored strain energy S are proportionally scaled by s.

5. Numerical examples

We optimize an eight-unit tensegrity lattice as shown in Figure 1. The material of all members (including bars and cables) is steel with Young's modulus E ($= 2.05 \times 10^5$ N/mm²). The yield stress of the bars is 500 N/mm², and that of the cables is assumed to be sufficiently large so that cables remain in elastic range. The nominal volume of the tensegrity lattice is assigned as 0.032 m³, and consequently, the bar length is about 170 mm. The radius of gyration around the week axis of the bars with rectangular section is assumed to be 0.3 mm; i.e., the thickness t is 1.04 mm, so that elastic buckling occurs before yielding.

In the examples, we adopt $\gamma = 16$ for approximation of the perfectly bilinear axial force-deformation relation as shown in Figure 6. The blue chain line shows variation of the non-dimensional axial force $\tilde{p}(\eta)$ with respect to the non-dimensional axial deformation η for a bar. The variations of non-dimensional strain energy $\tilde{w}(\eta)$ and stiffness $\tilde{k}(\eta)$ with respect to the non-dimensional axial deformation η for the same bar are plotted as solid red and dotted green lines respectively.
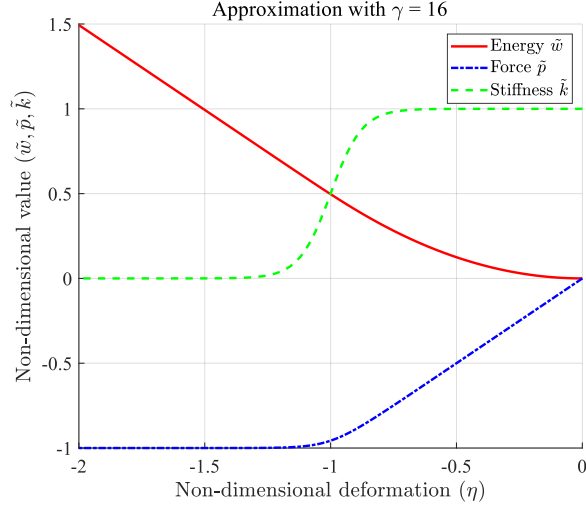
Figure 6. Variations of the non-dimensional approximated axial force $\tilde{p}$, strain energy $\tilde{w}$, and stiffness $\tilde{k}$ with respect to the non-dimensional axial deformation η ($\gamma = 16$).

In the bottom plane, Z-directional displacement is constrained at all nodes, X- and Y-directional displacements are constrained at one node, and X- or Y-directional displacement at two other nodes is constrained. This way, rigid-body motions of the tensegrity lattice are constrained allowing uniform expansion of the bottom squares. On the other hand, the 16 nodes in the top plane are enforced to move downward in the negative Z-direction with the same magnitude without displacement constraints in X- and Y-directions; thus, the top squares can also expand uniformly. Forced displacement in the negative Z-direction is applied incrementally with the constant increment 0.2 mm at each loading step. Deformation of the structure is computed using displacement increment method, and the unbalanced forces are reduced using Newton iteration.

In the large-deformation analysis in this study, the compressive behavior of a bar is computed using the relation presented in Section 3.2, while tension in the bar is allowed. Slackening of cables is checked after the optimization procedure. Tangent stiffness matrix is derived as sum of the linear stiffness matrix and the geometrical stiffness matrix [1]. The maximum stress of each bar after buckling is computed using Eq. (25), and the incremental step is terminated when the yield condition in Eq. (26) is violated. Strain energy stored in the members is computed from Eqs. (12) and (18).

As noted in Section 2, each truncated octahedral unit is super-stable when $-1 < q_b < 0$ while q_e is fixed at 1.0. Therefore, the parameter q_b is varied as –0.3, –0.4, –0.5, –0.6, –0.7, and

15

−0.8. The specified total material volume of members is 2.2687×10^3 mm³. The lower and upper bounds of the stress level β are 0.01 and 2.0, respectively. The lower and upper bounds of cross-sectional areas are 1.0 and 50.0 mm², respectively, for the bars, and 0.1 and 5.0 mm², respectively, for the cables. The optimization problem is solved using sequential quadratic programming available as the function *fmincon* in the optimization toolbox of MATLAB R2018a. Sensitivity coefficients of the objective function are computed using finite difference approximation.

Optimal solutions as well as the optimal objective values are listed in Table 1 for various values of q_b. The final vertical downward displacement *d*, when the maximum stress reaches the yield stress, is also shown in Table 1 for each optimal solution. The cross-sectional area of cables has its lower-bound value for almost all cases except for $q_b = -0.7$ and −0.8, and the cross-sectional area of bars increases as q_b is decreased. There is no obvious relation between the stress level and the objective function value; however, both of them have the largest values for the case of $q_b = -0.6$, and both of the values for $q_b = -0.2$ are larger than those for $q_b = -0.3$. The deformed shapes of the optimal solutions are shown in Figure 7. As indicated in Table 1, the total length L_b of bars decreases as q_b decreases; accordingly, the squares at the truncated vertices of the octahedron become smaller and the angle between a bar and Z-axis becomes smaller; consequently, the initial stiffness increases.

Table 1: Optimization results for different shapes of the tensegrity lattice.

q_b	L_b (10^4mm)	A_b (mm²)	A_c (mm²)	β	S (Nmm)	d (mm)
−0.2	1.6683	4.1038	0.1000	0.4315	1452.5	47.8
−0.3	1.5682	4.3688	0.1000	0.4222	719.2	34.2
−0.4	1.4734	4.6536	0.1000	0.5159	732.8	49.8
−0.5	1.3873	4.9467	0.1000	0.5693	1943.4	49.8
−0.6	1.3114	5.2374	0.1000	0.5823	3098.4	48.8
−0.7	1.2453	5.4791	0.1403	0.2512	2215.4	30.4
−0.8	1.1865	5.7980	0.1005	0.3619	1952.6	20.8

Relation between the vertical downward displacement of the top nodes and the sum of vertical reaction forces are plotted in Figure 8. As seen from the figure, the vertical stiffness, which is indicated by the slope of the curve, mostly decreases as the downward displacement is increased, although hardening occurs for the optimal solutions with q_b close to −1. Furthermore, the maximum reaction force increases as q_b is decreased except for the case of $q_b = -0.3$. The

structure has a limit-point-type instability for $q_b = -0.8$; i.e., it has a snap-through behavior if the deformation is controlled by the vertical load instead of the vertical displacement. Discontinuity in the tangent stiffness occurs when a bar buckles.

The maximum and minimum axial forces of each type of members are plotted with respect to the vertical displacement in Figure 9. Note that the axial force has positive value in tensile state. The green lines are the axial forces that take the maximum or minimum values after undergoing some amount of deformation. The number of buckled bars increases as vertical displacement is increased. However, the maximum and minimum axial forces do not change so much in the large deformation range, which means that the increase of reaction force in Figure 8 is due to the geometrical effect such as change in the member directions. Although we do not consider slackening or yielding of cables, the cable forces have non-smooth distributions, which is caused by buckling of bars.

The strain energy stored in cables, bars, and all members are respectively plotted with respect to the vertical displacement in Figure 10. It can be observed that the strain energy in the bars has a small proportion compared to that in the cables in the early stage before buckling, and the proportion increases rapidly after buckling. At the final stage where one of the bars yields, the strain energy in the bars is much greater than that in the cables, ranging from 1.47 ($q_b = -0.8$) to 7.25 ($q_b = -0.2$) times, although there are much less bars than cables.

The minimum eigenvalue of the tangent stiffness matrix is plotted with respect to the vertical displacement in Figure 11 to evaluate the stiffness in the weakest direction. The minimum eigenvalue of the tangent stiffness matrix is positive, showing that the structure is stable during the enforced displacement, except for the case of $q_b = -0.8$: there exists a nearly-zero eigenvalue, when the vertical displacement is 14.6 mm and the reaction force achieves its largest value. The displacement mode of the structure corresponding to this nearly-zero eigenvalue is shown in Figure 12 with an arrow at each node. It can be observed that most of the nodal displacements are almost perpendicular to the vertical enforced displacement, showing a bifurcation type buckling could occur at this point.

Figure 13 shows the relation between forced displacement and reaction force in the horizontal direction at the nodes in the top plane. The horizontal displacement in the negative *X*-direction is

applied at the top nodes after enforcing 20 mm vertical displacement. For the cases with $q_{\mathrm{b}} = -0.2$ and -0.3 in Figures 13(a) and (b), analysis terminated due to bar yielding, while for the cases with $q_{\mathrm{b}} = -0.5$ and -0.7 in Figures 13(c) and (d), analysis terminated due to instability in the range of small horizontal deformation. Therefore, the optimized tensegrity lattice after vertical deformation has positive horizontal stiffness when the force density of bars is sufficiently large (negative with small absolute value). However, horizontal stiffness may be lost when q_{b} is small due to shear deformation of the upper and lower units.

6. Conclusions

An optimization method has been presented for tensegrity lattices composed of eight truncated octahedral units, in which the stored strain energy before a bar yields under forced vertical displacement is maximized under constraints on the structural material volume.

A new formulation is presented for the relation between the axial compressive force and displacement of a bar using dilogarithm function for smoothing the discontinuity due to buckling. The maximum edge stress after buckling is estimated assuming the lateral displacement in sinusoidal shape. Thus, the constraint on the yielding of bar is implicitly incorporated in the optimization problem by terminating the analysis when yielding occurs in a bar. As a result of uniformly scaling the optimal solution to a specific size, energy absorption by the structure is scaled in a cubic manner.

It has been shown in the numerical examples that a flexible structure with degrading vertical stiffness is obtained as a result of optimization. Although structures generally retain compression stiffness even after large deformation, in some cases a bifurcation buckling in the horizontal direction may occur due to loss of stiffness for shear deformation of the units. The variations of axial forces and strain energy against vertical displacement are also investigated to clarify the mechanism of degrading stiffness. Although the axial forces in the members become almost constant in the large deformation, the reaction force increases due to the change of directions of members. The strain energy is stored mostly in cables when the deformation is small, and the bars have much greater contribution to energy absorption in the large deformation range, emphasizing the advantage in considering bar buckling for energy absorption purpose.

It has been confirmed in the numerical examples that the optimized tensegrity lattice after vertical deformation has positive horizontal stiffness when the force density of bars is sufficiently large (negative with small absolute value). In this way, a tensegrity lattice with flexibility in vertical direction and adequate horizontal shear stiffness can be obtained for application as an isolation system mitigating vibration of the structure against vertical motion.

Finally, our study was limited to the behavior of an 8-unit elementary lattice, due to its ability to tile the entire 3-dimensional space. Further research should investigate if lattice size-effects are present.

Acknowledgements

References

[1] J. Y. Zhang and M. Ohsaki, *Tensegrity Structures: Form, Stability, and Symmetry*, Mathematics for Industry 6, Springer, 2015.

[2] J. Y. Zhang and M. Ohsaki, Adaptive force density method for form-finding problem of tensegrity structures, *Int. J. Solids and Struct.*, Vol. 43(18-19), pp. 5658-5673, 2006.

[3] J. Y. Zhang and M. Ohsaki, Stability conditions for tensegrity structures, *Int. J. Solids and Struct.*, Vol. 44(11-12), pp. 3875-3886, 2007.

[4] R. E. Skelton and M. C. de Oliveira, *Tensegrity systems*, Springer, 2009.

[5] J. J. Rimoli, A reduced-order model for the dynamic and post-buckling behavior of tensegrity structures, *Mechanics of Materials*, Vol. 116, pp. 146–157, 2018.

[6] V. SunSpiral *et al*., Tensegrity based probes for planetary exploration: Entry, descent and landing (EDL) and surface mobility analysis, *International Journal of Planetary Probes*, 7(13), 2013.

[7] N. B. H. Ali and I. F. C. Smith, Dynamic behavior and vibration control of a tensegrity structure, *Int. J. Solids Struct.*, Vol. 47, pp. 1285-1296, 2010.

[8] M. Goyal, E. A. P. Hernandez and R. E. Skelton, Analytical study of tensegrity lattices for mass-efficient mechanical energy absorption, *Int. J. Space Structures*, Vol. 34(1-2), pp. 3-21, 2019.

[9] J. J. Rimoli and R. K. Pal, Mechanical response of 3-dimensional tensegrity lattices, *Composites Part B*, Vol. 115, pp. 30–42, 2017.

[10] L.-Y. Zhang *et al*., Automatically assembled large-scale tensegrities by truncated regular polyhedral and prismatic elementary cells, *Composite Structures*, Vol. 184, pp. 30-40, 2018.

[11] X.-Q. Feng *et al*., Design methods of rhombic tensegrity structures, *Acta Mech. Sin.*, Vol. 26, pp. 559-565, 2010.

[12] F. Fabbrocino and G. Carpentieri, Three-dimensional modeling of the wave dynamics of tensegrity lattices, *Composite Structures*, Vol. 173, pp. 9-16, 2017.

[13] K. Caluwaerts *et al.*, Design and control of compliant tensegrity robots through simulation and hardware validation, *Journal of the Royal Society Interface*, Vol. 11(98): 20140520, 2014.

[14] H. Salahshoor, R. K. Pal and J. J. Rimoli, Material symmetry phase transitions in three-dimensional tensegrity metamaterials, *Journal of the Mechanics and Physics of Solids*, Vol. 119, pp. 382-399, 2018.

[15] R. K. Pal, M. Ruzzene and J. J. Rimoli, Tunable wave propagation by varying prestrain in tensegrity-based periodic media, *Extreme Mechanics Letters*, Vol. 22, pp. 149-156, 2018.

[16] Y. Chen, J. Feng and Y. Wu, Novel form-finding of tensegrity structures using ant colony systems, *J. Mech. Rob.* ASME 4 (031001), 2012.

[17] M. Ohsaki and J.Y. Zhang, Nonlinear programming approach to form-finding and folding analysis of tensegrity structures using fictitious material properties, *Int. J. Solids Struct.*, Vol 69-70, pp. 1-10, 2015.

[18] J. Y. Zhang, M. Ohsaki and F. Tsuura, Self-equilibrium and stability of regular truncated hexahedral and octahedral tensegrity structures, Vol. 161, pp. 182-192, *Int. J. Solids Struct.*, 2019.

[19] L.-Y. Zhang, Y. Li, Y.-P. Cao, X.-Q. Feng and H. Gao, Self-equilibrium and super-stability of truncated regular polyhedral tensegrity structures: A unified analytical solution, *Proc. Royal Soc. A*, Vol. 468, pp. 3323-3347, 2012.

[20] L. Zhang, C. Zhang, X. Feng and H. Gao, Snapping instability in prismatic tensegrities under torsion, *Appl. Math. Mech. -Engl. Ed.*, Vol. 37(3), pp. 275-288, 2016.

[21] M. A. Fernández-Ruiz, E. Hernández-Montes, J. F. Carbonell-Márquez and G. M. Gil-Martin, Octahedron family: The double-expanded octahedron tensegrity, *Int. J. Solids Struct*, Vol. 165, pp. 1-13, 2019.
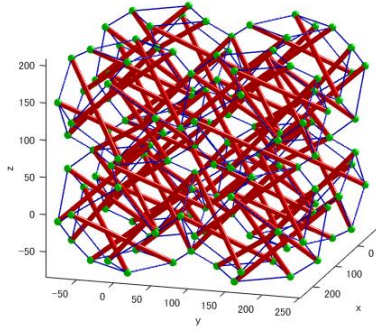
(a) $q_b = -0.3$
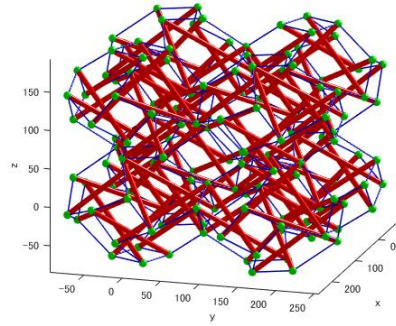
(b) $q_b = -0.5$
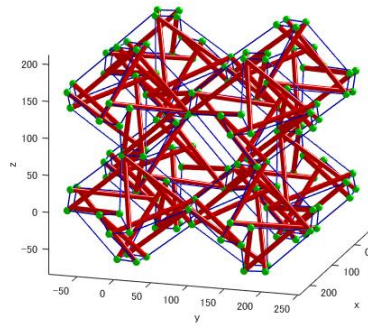
(c) $q_b = -0.7$

Figure 7:   Deformed shape of optimal solutions.
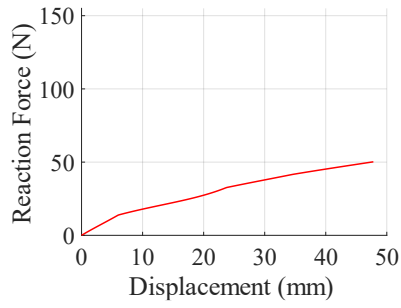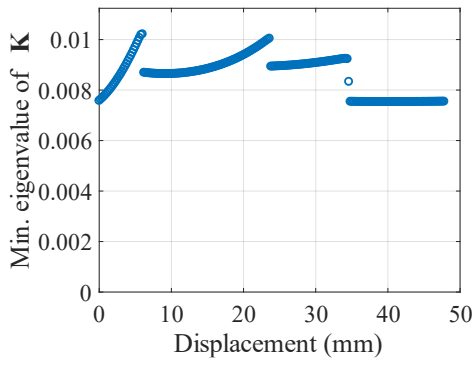
(a) $q_b = -0.2$
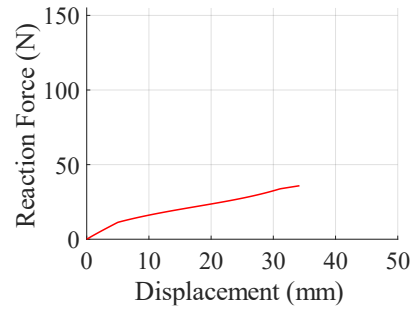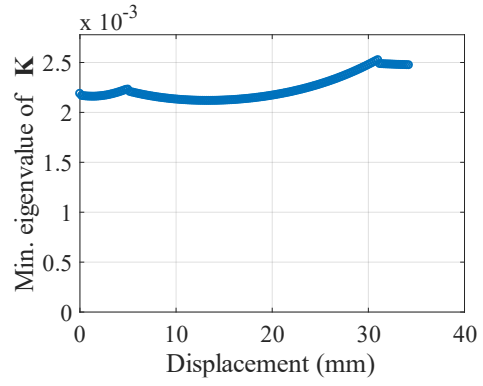
(b) $q_b = -0.3$
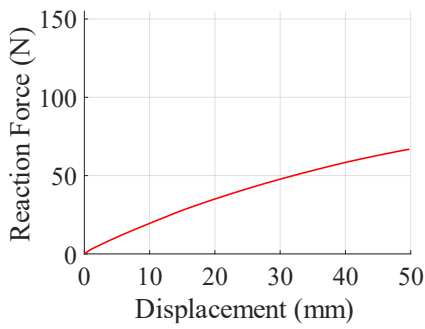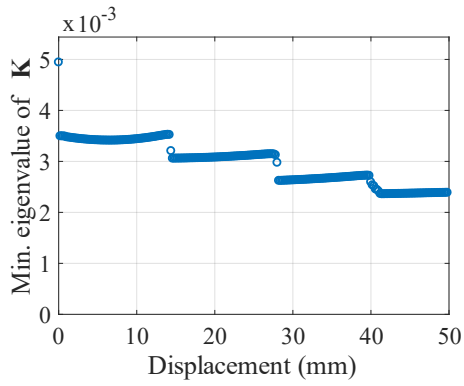
(c) $q_b = -0.5$
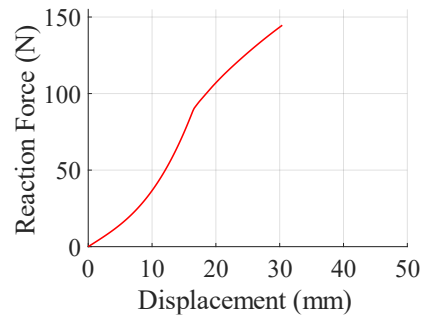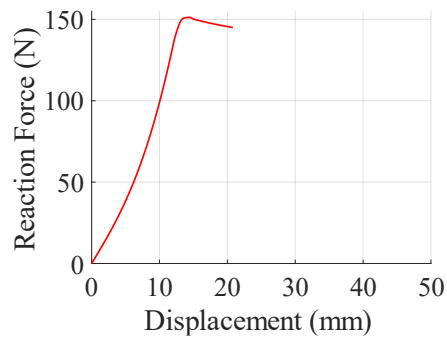
(d) $q_b = -0.7$

(e) $q_b = -0.8$

Figure 8: Relation between vertical displacement and reaction force.
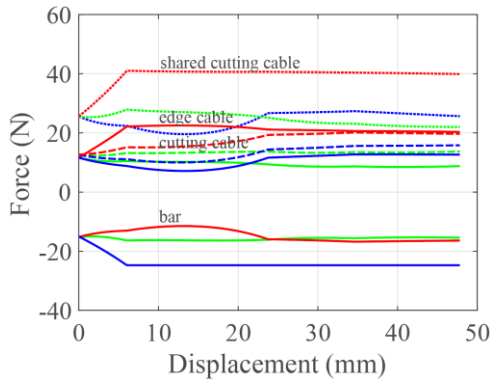
(a) $q_b = -0.2$
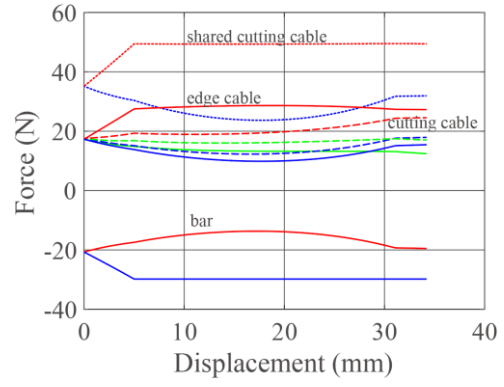
(b) $q_b = -0.3$
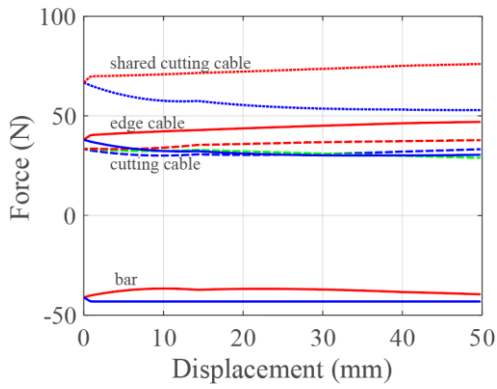
(c) $q_b = -0.5$
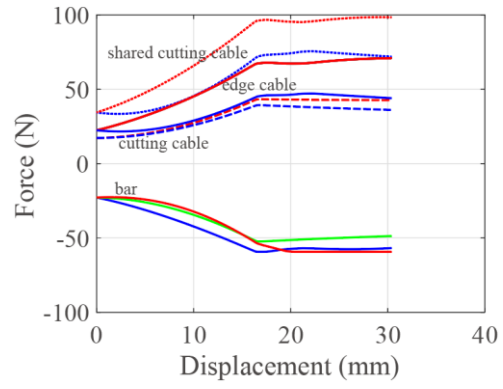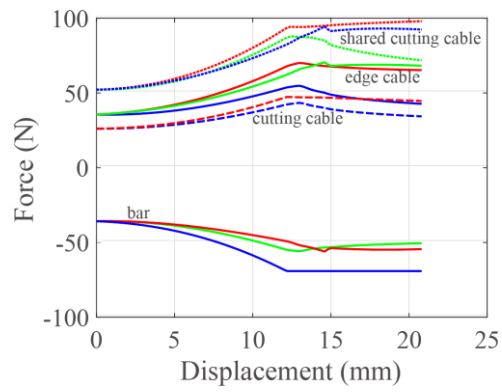
(d) $q_b = -0.7$

(e) $q_b = -0.8$

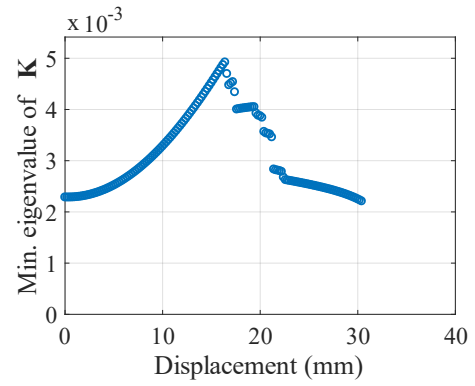Figure 9: Relations between vertical displacement and member forces.
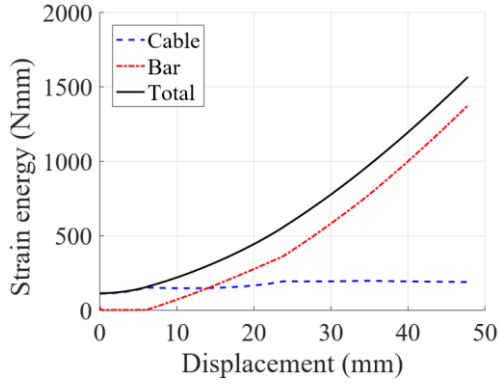
(a) $q_b = -0.2$
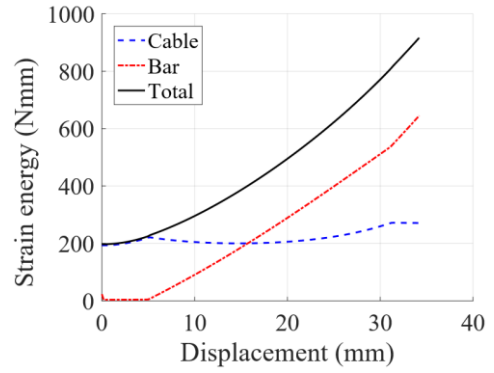
(b) $q_b = -0.3$
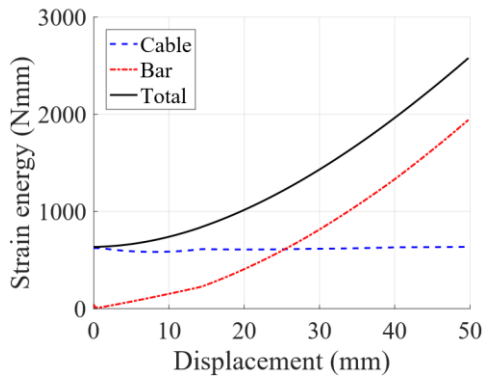
(c) $q_b = -0.5$
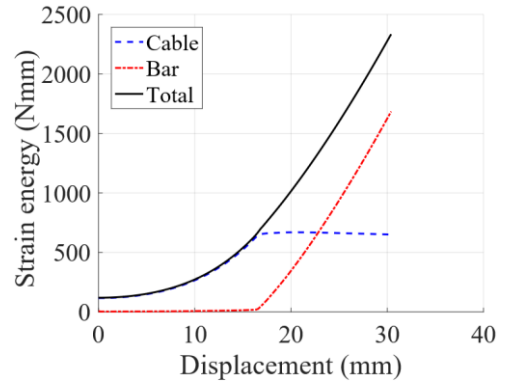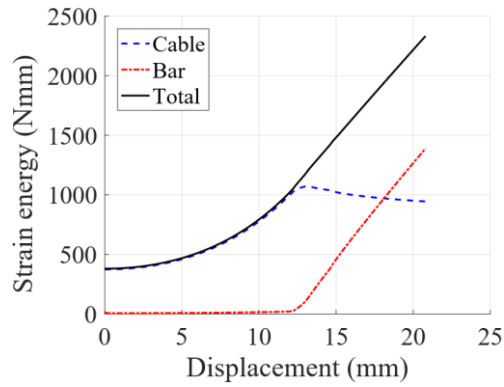
(d) $q_b = -0.7$

(e) $q_b = -0.8$

Figure 10:   Relation between vertical displacement and strain energy.
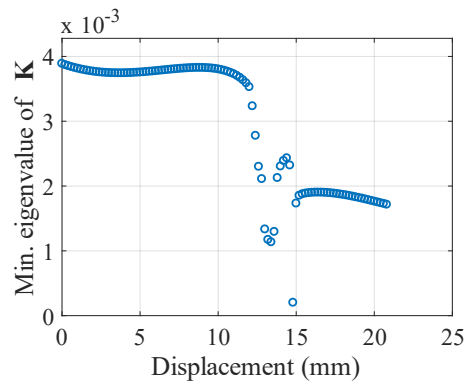
(a) $q_b = -0.2$

(b) $q_b = -0.3$

(c) $q_b = -0.5$

(d) $q_b = -0.7$

(e) $q_b = -0.8$

Figure 11: Relation between vertical displacement and minimum eigenvalue of tangent stiffness matrix.
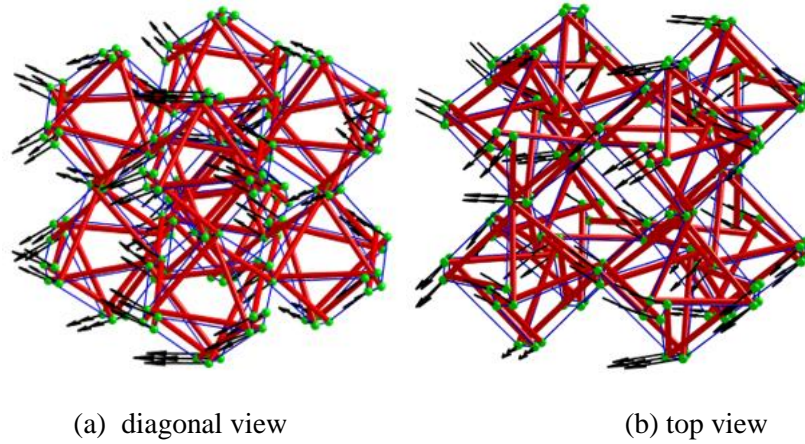
(a) diagonal view   (b) top view

Figure 12: Displacement mode corresponding to the nearly-zero eigenvalue of tangent stiffness

for $q_b = -0.8$.

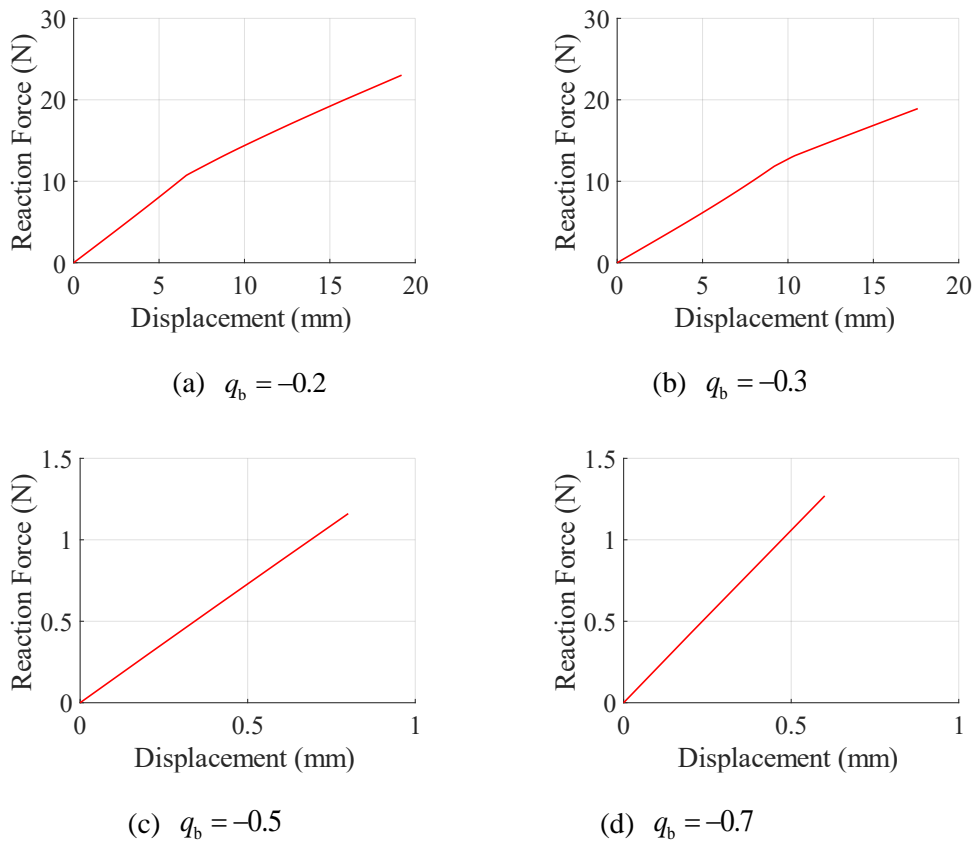(a) $q_b = -0.2$ (b) $q_b = -0.3$

(c) $q_b = -0.5$ (d) $q_b = -0.7$

Figure 13: Horizontal displacement and horizontal reaction force.